Chapter 6

Polymer:2-D Material Composite for High Performance Flexible Devices: Part-I

In the recent times, research on 2-dimensional (2-D) materials based devices particulary for the flexible devices, have grown tremendously owing to their excllent mechanical strength against tensile and compressive strain. Moreover, 2-D materials such as graphene oxide and molybdnum disulfide have proven record of demonstrating excellent resistive switching behavior on the rigid as well as the flexible substrate. This chapter will explain the resistive switching behavior of PVP:MoS_2 composite and HfO_x bilayer based flexible hybrid RRAMs. Devices have exhibited excellent memory window at remarkably low switching voltages. Also, the devices withstand the external tensile and compressive strain under extreme bending conditions [Varun *et al.*, 2020a].

6.1 GRAPHENE OXIDE COMPOSITES for RRAMs

The demand for high-performance flexible nonvolatile memories has escalated to new highs with applications extending to flexible and wearable electronics, healthcare, computation, radio frequency identification (RFID) tags, foldable displays, sensors, and data storage [Ielmini, 2016; Ielmini and Wong, 2018; Lee *et al.*, 2014; Zhao *et al.*, 2018b] . The resistive random access memory (RRAM) devices, a class of nonvolatile memories, have emerged as the game changer in the field of flexible electronics with tremendous capabilities such as high mechanical strength, flexibility, transparency, low power consumption, fast switching speed, miniaturization capabilities, and compatibility with CMOS technology [Lanza *et al.*, 2019]. The incorporation of various transparent and flexible dielectric materials and conductive electrodes in RRAMs has proven its capability for future high density flexible data storage devices and flexible logic circuits [Kang *et al.*, 2017]. Operation of RRAMs is based on the physical phenomenon of resistive switching (RS), which is the capability of selective organic, metal oxides, perovskites, and low-dimensional dielectric materials to demonstrate multiple electrical resistance states namely high and low resistance states (HRS and LRS respectively), regulated under the effect of an external bias [Hui *et al.*, 2017; Ielmini, 2016; Kang *et al.*, 2017; Kim *et al.*, 2019a]. Among the category of materials mentioned above, the most reliable and promising switching characteristics under various mechanical stress, strain, and stretchable conditions have been showcased by metal oxides and organic 2-dimensional (2D) materials [Saini *et al.*, 2018; Sassine *et al.*, 2019; Siddiqui *et al.*, 2017; Zhou *et al.*, 2018]. Recently, graphene and its derivatives like graphene oxide (GO) and reduced graphene oxide (rGO) attracted profound research interest due to their excellent conducting, dielectric, mechanical, and semiconducting properties which are being exploited in applications mainly focused towards memories and sensors [Bhati *et al.*, 2018; Kim *et al.*, 2019b; Qi *et al.*, 2018; Shi *et al.*, 2018]. The presence of charge trapping and charge donating functional groups like –OH and C = O and defect sites govern the charge transport between the single layer and multilayered stacks of GO [Kumar *et al.*, 2016]. However, the RS

phenomenon in GO and its derivatives is still debatable and obscure, as reports available so far couldn't distinctly elaborate its origin [Kim *et al.*, 2018; Saini *et al.*, 2018; Shi *et al.*, 2018; Zhao *et al.*, 2018b]. Despite this, composites of organic dielectrics and GO are an attractive choice for flexible RRAM fabrication due to the feature of feasible low-temperature deposition with facile methods like spin coating, dip coating, drop cast, inkjet printing, and electrochemical methods [Kim *et al.*, 2019b; Qi *et al.*, 2018; Zhao *et al.*, 2018b]. However, higher switching voltages, poor cyclic endurance, and low sample yield remained some vital issues of concern in corresponding devices which needed attention [Hui *et al.*, 2017; Lanza *et al.*, 2019]. Moreover, most of these devices were realized on rigid platforms, without any outlook for their feasibility and stability on flexible substrates.

For high performance flexible device applications, GO can be an excellent choice, as it can easily be synthesized from graphene using economical methods such as Hummer's method [Hummers and Offeman, 1958] and thermal reduction [Kumar *et al.*, 2016] and has excellent capabilities to alleviate the aforementioned concerns presented by rigid RRAM devices and simultaneously providing them electrical stability under mechanically stressed conditions. In this paper, a PVP:GO/HfO_x active layer based flexible RRAM has been demonstrated with excellent repeatability and memory window. Adoption of composite dielectrics and bilayer structures in active layer of RRAM have shown to control the unregulated and randomly oriented growth of conductive filaments, occurrence of which tends to deteriorate RRAM performance. The Hafnium oxide (HfO_x) has already proven its tremendous capabilities in RRAM performance where the flexibility, miniaturization, lower power consumption, highly reliable, and CMOS compatibility are some of its key highlights [Shang *et al.*, 2017]. The incorporation of HfO_x as a secondary active layer in these RRAM devices has enhanced their performance by providing superior control over filament formation and rupture. Thin film of PVP:GO composite has been integrated as the secondary active layer in the RRAM configuration to harness the combined advantages of the hybrid composite structure of PVP and GO such as lower leakage current and better mechanical strength. The composite of PVP and varied concentration of GO over the HfO_x thin film has resulted in a noticeable improvement in the device performance with impressive sample yield in comparison to previous reports [Varun *et al.*, 2018]. Along with DC endurance of over 800 cycles and I_{on}/I_{off} of $>10^5$, all the fabricated devices were found to be functional, demonstrating a 100% sample yield, a definite improvement in comparison to PVP and HfO_x active layer based RRAM devices [Shang *et al.*, 2017; Sun and Wen, 2019; Varun *et al.*, 2018]. Finally, the devices were subjected to extreme bending conditions (up to bending radius of 2.5 mm) and providing 150 cycles of consecutive tensile and compressive strain. A memory window clearly distinguishing the two states was still maintained in both the switching and retention time characteristics despite the degradation caused by extreme mechanical strain. After undergoing excessive strain at bending radius of 2.5 mm, cracks were evolved at the bottom electrode surface, leading to irreversible loss of switching operation.

6.2 FABRICATION OF FLEXIBLE RRAMs

Firstly, the Ag/PVP:GO/HfO_x/ITO rigid RRAM devices were fabricated on ITO glass substrates. ITO glass substrates were cleaned using the ultrasonic bath in isopropyl alcohol (IPA), acetone, and methanol for 10 minutes each and finally dried with N_2 blow. Over the ITO, a 5 nm thin hafnium oxide (HfO_x) film was deposited at 100℃ using Savannah S200 atomic layer deposition (ALD) system using Tetrakis(dimethylamido)hafnium(IV) and water as precursors. To prepare the second dielectric layer of Poly(4-vinylphenol) (PVP) (M_w 25,000) and graphene oxide (GO) composite, the PVP and GO solutions were mixed in ratios of equal volume. A 2.5 wt.% PVP solution was prepared in IPA by ultrasonication for 30 minutes. Furthermore, 0.5 mg, 1 mg, 1.5 mg, and 2 mg of GO was dissolved in 1 ml of deionized water and sonicated for four hours, followed by probe sonication for 30 minutes for uniform dispersion of GO, and centrifuged for thirty minutes at 6000 rpm. Finally, the PVP and GO composite was prepared with mixing them dropwise and further sonicated for 30 minutes to prepare a properly dissolved solution. The solution was spin coated on the HfO_x at 4000 rpm for 45 seconds and afterwards left for

drying at 65 ℃ for one hour for complete solvent evaporation, yielding an overall active layer thickness of ~37 nm, ~43 nm, ~55 nm, and ~86 nm for solution with 0.5 mg/ml, 1 mg/ml, 1.5 mg/ml, and 2 mg/ml GO concentration respectively. Finally, a 150 nm thick Ag electrode was thermally evaporated through shadow mask having circular patterns with 250 µm diameter. The samples fabricated with 0.5 mg/ml, 1 mg/ml, 1.5 mg/ml, and 2 mg/ml GO concentration in 2.5 wt.% PVP and 5 nm HfO_x were named as Device-A (Dev.A), Device-B (Dev.B), Device-C (Dev.C), and Device-D (Dev.D) respectively.

The flexible Ag/PVP:GO/HfO_x/ITO/PET were fabricated using the same fabrication method and sequence used for Dev.B. The electrical characterization of devices was carried out using Keithley 4200 SCS with potential applied at top electrode (TE) and bottom electrode (BE) kept at ground potential. The surface morphology of PVP:GO films was analyzed using XE70 atomic force microscopy (AFM) by Park Systems. FTIR Spectrum 2 by Perkin Elmer in ATR mode was used to study different chemical bonds, functional groups, and defects present in the nanocomposite film. Structural analysis of the PVP:GO composite was performed using AIRIX STR 500 Raman spectroscopy technique.

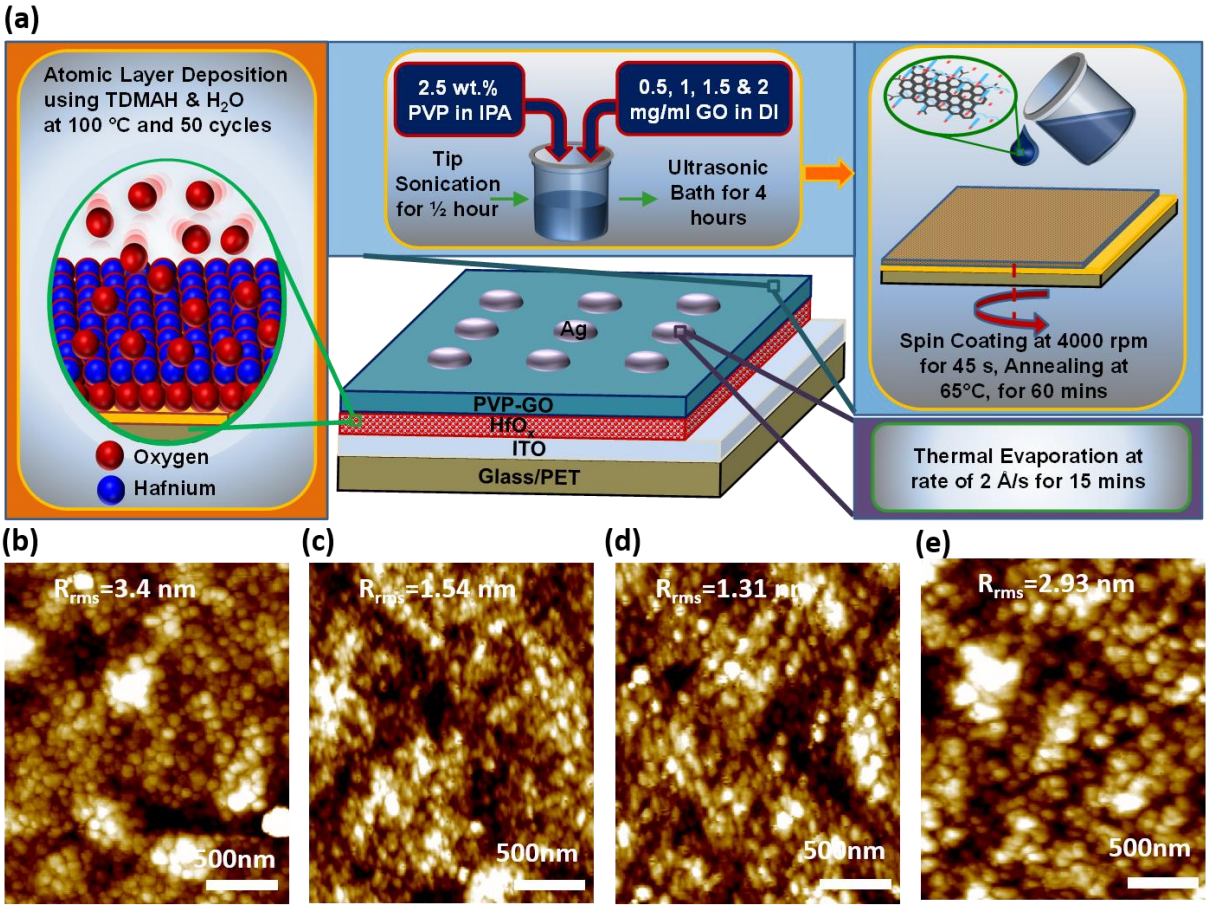

Figure 6.1: (a) Device schematic and fabrication process of each layer with their processing conditions, **(b-e)** AFM images of Dev.A, Dev.B, Dev.C, Dev.D respectively with 2µm × 2µm scan area representing the root mean square roughness of each sample.

6.3 RESULTS & DISCUSSIONS

6.3.1 PVP:GO Film & Material Characterization

Figure 6.1(a) shows the device schematic along with the fabrication steps of each layer, their processing conditions, and the device schematic. Figure 6.1(b-e) shows the structural topography of PVP:GO composite with 0.5 mg/ml, 1 mg/ml, 1.5 mg/ml, and 2 mg/ml GO

concentration respectively, studied with AFM operated in non-contact tapping mode which shows a root mean square (RMS) roughness of 3.4 nm, 1.54 nm, 1.31 nm, and 2.93 nm respectively, signifying overall smooth films, which is mainly due to PVP part of the solution, known to produce smooth films. Figure 6.2(a) signifies the two signature D (1338 cm^{-1}) and G (1612 cm^{-1}) bands of GO in the Raman spectroscopy, indicating the existence of sp^3 and sp^2 hybridized carbon respectively in the GO. The intensity of D and G bands is strengthening with increasing GO concentration in the PVP:GO film. The Raman spectra of composite film also specifies the presence of PVP with peaks at 642 cm^{-1}, 843 cm^{-1}, and 1198 cm^{-1} alongwith the tangential mode peak at 1446 cm^{-1} [Paul *et al.*, 2005; Saini *et al.*, 2018]. The structural variations with the changing GO concentration in the PVP:GO solution is studied using the fourier transform infrared (FTIR) spectroscopy where different functional groups were categorized using vibrational modes in the material. Figure 6.2(b) shows the FTIR spectra of PVP:GO films indicating various characteristic peaks at 758 cm^{-1}, 906 cm^{-1}, 1068 cm^{-1}, 1508 cm^{-1}, and 1600 cm^{-1} which confirms the presence of

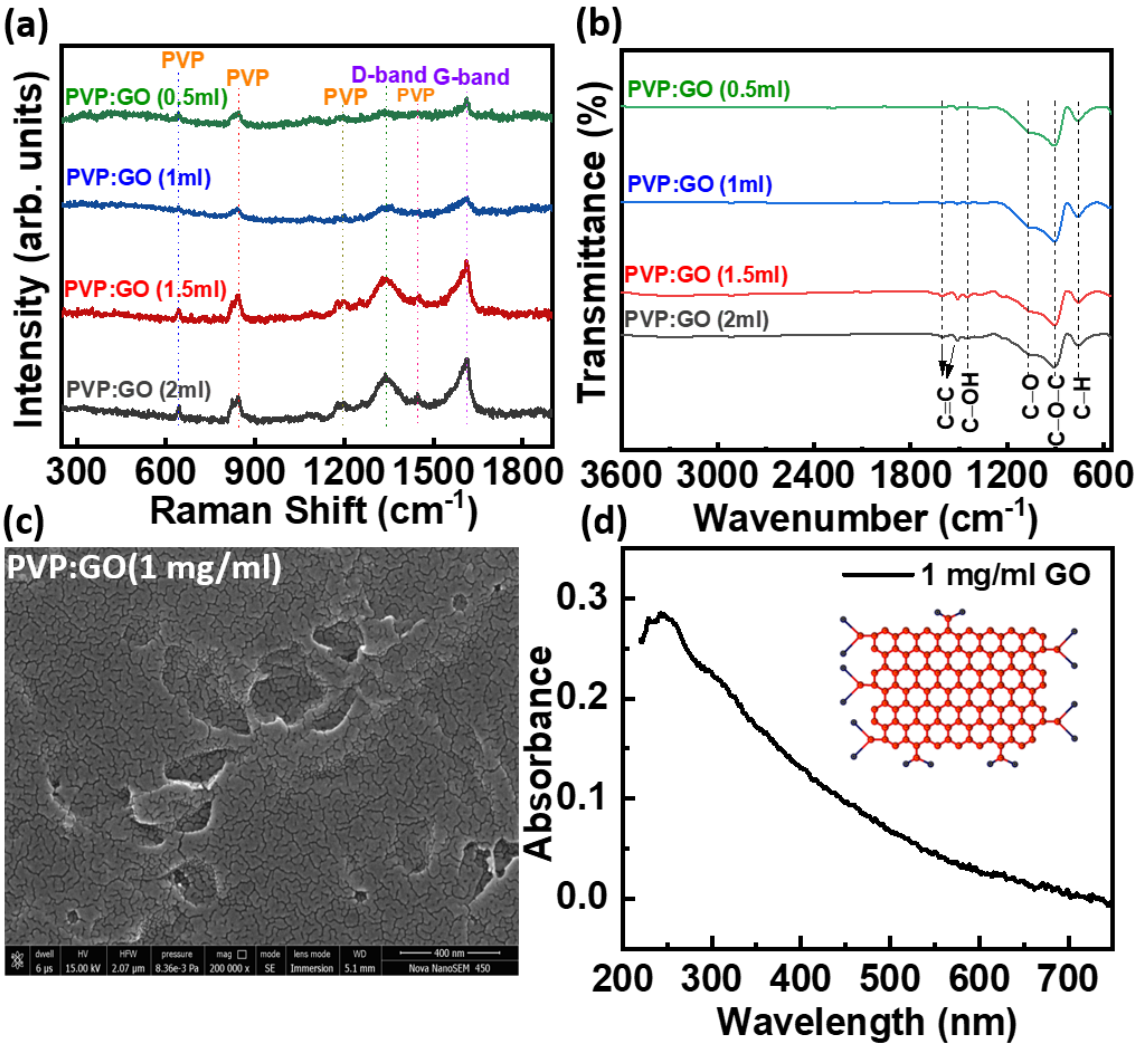

Figure 6.2: (a) The Raman spectroscopy of PVP:GO with different GO concentrations indicating the presence of signature D and G bands of GO at 1338 cm^{-1} and 1612 cm^{-1} alongwith the four peaks of PVP, **(b)** FTIR spectroscopy of PVP:GO film with different GO concentrations indicating different functional groups attached GO sheets and PVP, **(c)** the FESEM topography of PVP:GO composite over HfO_x film, and **(d)** the UV-visible spectroscopy of 1 mg/ml GO solution. Inset shows the molecular structure of GO with different functional groups attached.

of –C–H, –C–O–C (epoxy), –C–O, benzene ring framework, and –C=C respectively, suggesting the presence of highly pure GO sheets in the film. The primary peak around 3400 cm^{-1}representing the –OH group present in GO and PVP, remains absent in all concentrations. However, the peak at 1372 cm^{-1} exhibits the presence of hydroxyl and carboxylic groups, and

water in the GO sheets [Krishnamoorthy *et al.*, 2013; Thiounn *et al.*, 2018; Varun *et al.*, 2018]. The intensity of all the peaks rises with the increasing GO concentration. Figure 6.2(c) confirms the morphology of uniformly distributed PVP:GO composite over the HfO_x surface using FESEM characterization, demonstrating the inherent layered structure of GO. The UV-visible spectra of GO shown in Figure 6.2(d) demonstrates an absorption peak at 242 nm has primarily occurred due to π- π* transition in C-C aromatic ring [Lai *et al.*, 2012].

6.3.2 Electrical Performance Of Flexible RRAMs

The electrical characterization of devices is carried out by applying a continuous sweep voltage pulse of $-V_{max} \rightarrow 0 \rightarrow V_{max} \rightarrow 0 \rightarrow -V_{max}$. The memory performance of all the samples was examined by different electrical characterization techniques. The effect of varying the GO concentration on RS behavior of the device has been shown in Figure 6.3(a) where an excellent

Table 6.1 Summary of switching parameters of Ag/PVP:GO/HfO_x/ITO RRAM device.

Parameter	Dev.A	Dev.B	Dev.C	Dev.D
V_{set} (V)	0.72	0.64	0.54	0.58
V_{reset}	-2.22	-2.42	-1.6	-1.98
I_{on}/I_{off}	1×10^5	3.3×10^5	7.4×10^3	8.3×10^4

bipolar resistive switching is observed in the initial cycles with a decent memory window of ~10^4-10^5 in all four samples. While maintaining almost similar V_{set} ranging from 0.54 V to 0.72 V, the V_{reset} demonstrated broader spectrum of -1.6 V to -2.42 V mainly due to varied filament dimensions and random rupture processes. Similarly, the data retention characteristic of all samples was examined by applying a constant bias of 0.2 V in LRS and -0.2 V in HRS for 10^4 s. As shown in Figure 6.3(b), the devices demonstrated decent retention with nearly no degradation in current levels of both states. Interestingly, the I-V characteristic of Dev.A, Dev.C, and Dev.D demonstrated an improper reset process in subsequent cycles resulting in degraded I_{on}/I_{off} and can be observed in the retention time characteristics as well. The extracted switching and performance parameter from all the samples has been shown in Table 6.1. The switching performance of Dev.A was deteriorated due to thinner PVP:GO film in comparison to the other samples that resulted in reset failure and higher leakage current in devices. Dev.C and Dev.D demonstrated a higher current of 12.4 mA and 24.82 mA respectively at peak voltage of 1.5 V. A higher current during the RS process raises the temperature around the CF region (~1000 K – 1200 K) which increases the conductivity of GO [Becerril *et al.*, 2008; Bhati *et al.*, 2018; Kwon *et al.*, 2016; Liang *et al.*, 2009; Ma *et al.*, 2018; Vallés *et al.*, 2012; Yalon *et al.*, 2012; Yazdanparast *et al.*, 2015; Zhao *et al.*, 2018b]. Hence, at the higher GO concentration, the increased conductivity in the CF region will hinder the reset process and increases the leakage current [Kim *et al.*, 2016; Zhao *et al.*, 2018b]. However, the Dev.B outperformed with maintaining the excellent I_{on}/I_{off} of >10^5 throughout the retention test and in the switching characteristics due to optimized GO concentration in the film, film thickness and the lower peak current. Hence, Dev.B was selected for further RS investigation.

The study of RS behavior of Dev.B was investigated by current-voltage (*I*-*V*) characteristics of memory cells. All the pristine devices were initially non-conducting and a forming pulse of 3 V with 5 mA compliance current is applied that turned on the device at forming voltage V_f = 2.82 V. Compliance current limit was removed for further studies. Figure 6.3(c) shows the bipolar RS nature of the device when subjected to an electrical bias from -4 V to 2 V where the device shows a sharp rise in current at V_{set} = 0.64 V, exhibiting the set process by the formation of a conductive path between the TE and BE. The reset process occurs when the applied bias is swept to V_{reset} = -2.42 V, which is likely to be happening due to a fracture in the conductive path. Afterward, the DC endurance of the device was tested, where it exhibited 800 cycles of repeatable operation, as shown in Figure 6.3(d). The variation of set and reset current of

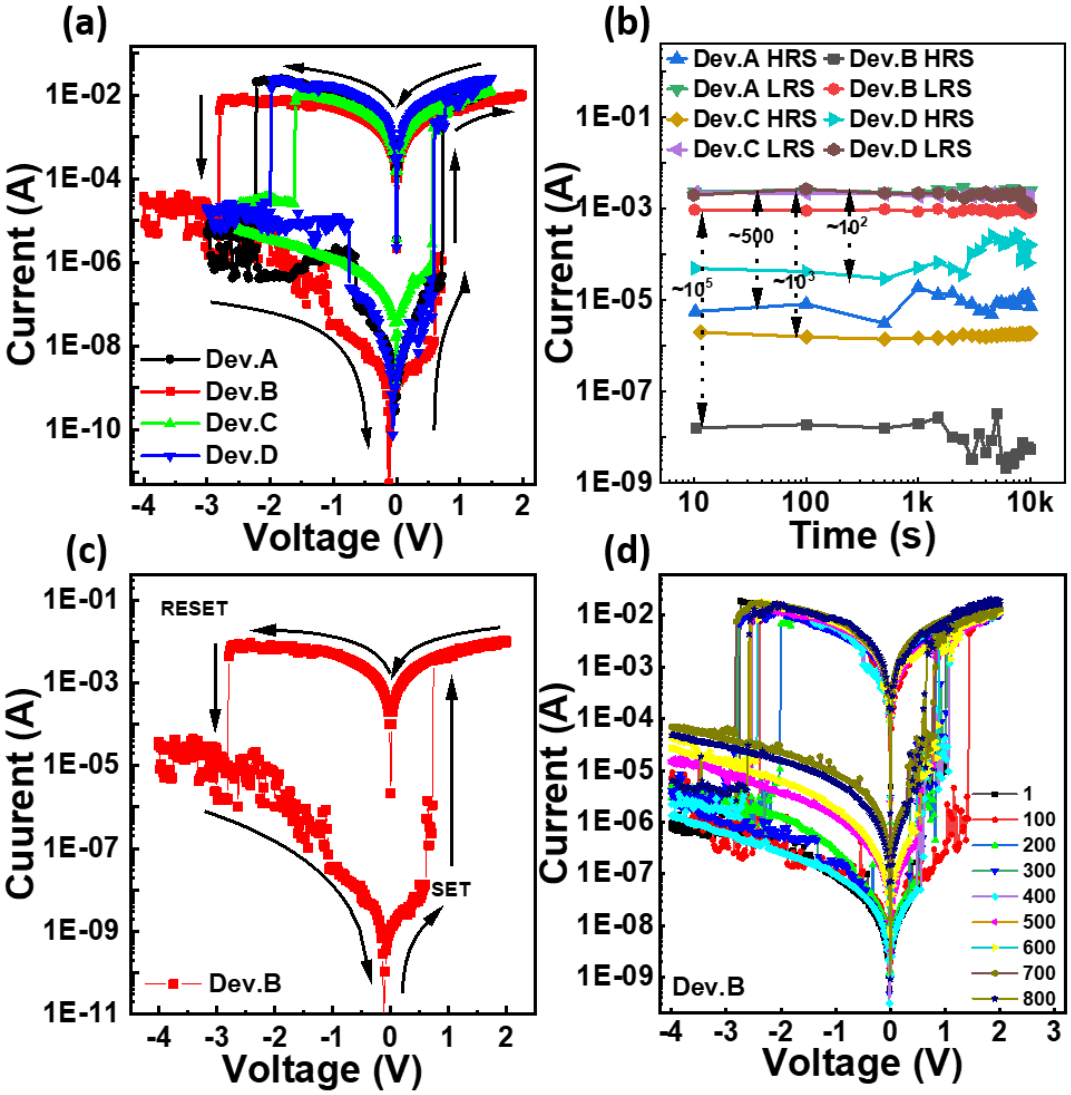

Figure 6.3: (a) Displays *I-V* characteristics of a device of all the four samples with different GO concentration, **(b)** retention time characteristics showing the I_{on}/I_{off} of all samples. This confirms degradation on I_{on}/I_{off} after initial I-V cycles, **(c)** switching characteristics of Dev.B with Vset and Vreset of 0.64 V and -2.42 V respectively, and **(d)** shows the DC endurance (repeatability) of Dev.B successfully exhibiting 800 cycles of switching operation.

800 cycles at 0.2 V read voltage in the LRS and HRS respectively is shown in Figure 6.4(a) where it displays an excellent memory window of $>10^5$ till 400 cycles and then a degradation of two orders of magnitude can be observed. This indicates a clear separation of $>10^3$ between the two states by the end of the cyclic operation, confirming that devices have capability to perform nonvolatile memory operations. The AC switching endurance has been an integral characteristic of all the memory devices where the device under test is exposed to a continuous voltage pulse with optimized amplitude and pulse width. In this case, an AC pulse of -4 V/2 V voltage levels with 20 ms pulse width was applied to test the continuous erase and write capability of device (pulse shown in inset of Figure 6.4(b)). No prominent degradation in the memory window for 1400 cycles was observed, again indicating a reliable and repeatable switching performance. The performance parameters such as retention time, and DC and AC cyclic endurances of the RRAMs in the current study have been mentioned in Table 6.2 and compared with other reported RRAMs based on GO and its nanocomposites. RRAMs in this study displays enhanced performance in comparison to its reported counterparts due to incorporation of efficient structural configuration and optimal GO concentration in the device.

Another tool which is widely used to analyze the reliability issues in microelectronics devices is Weibull's distribution $\ln\text{-}\ln(1\text{-}f(y) = \beta\ln(x)$ where β is the shape factor. A higher β signifies better

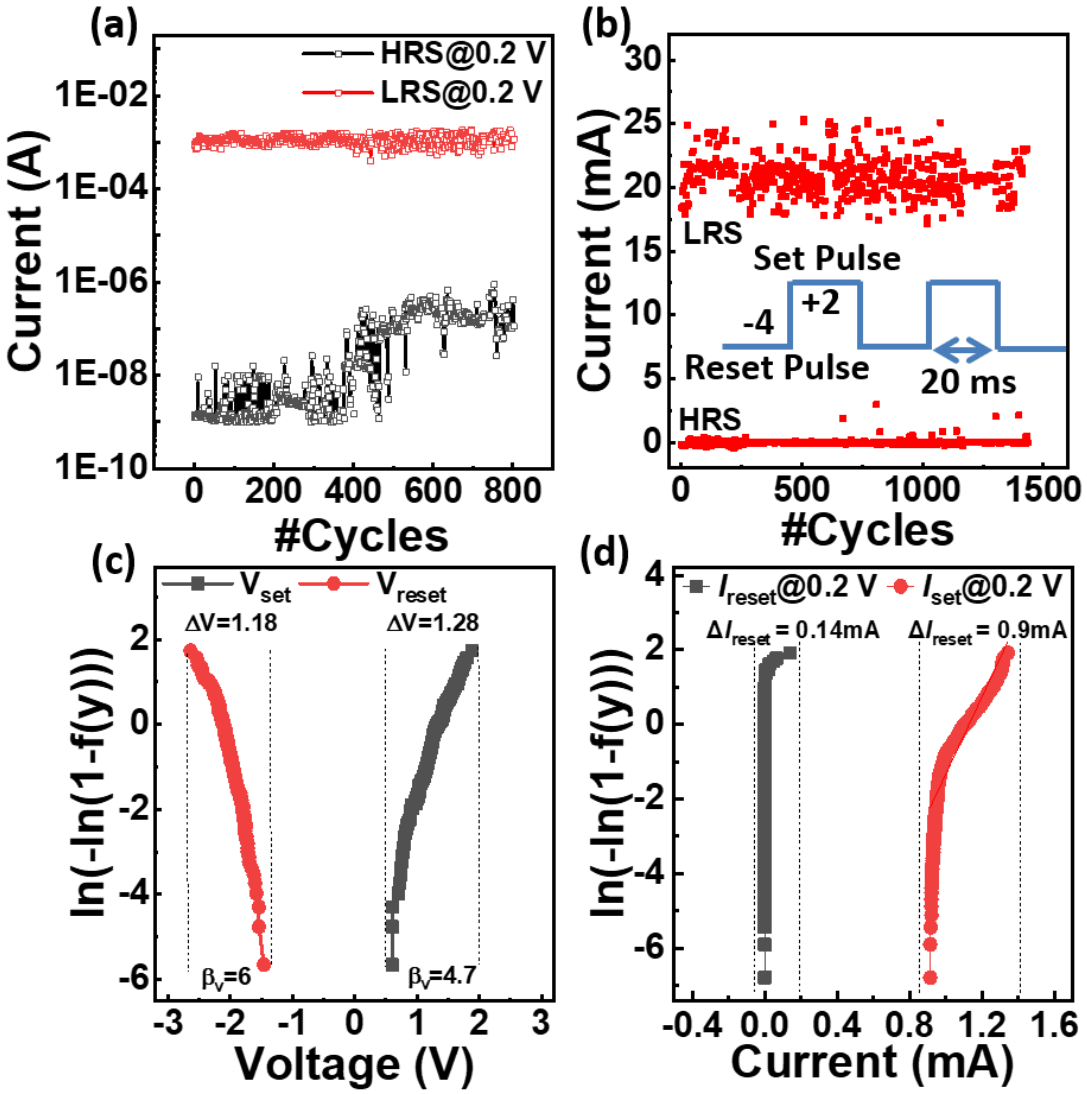

Figure 6.4: (a) The variation of HRS and LRS current at 0.2 V read voltage. A visible rise in HRS current after 400 cycles is observed, **(b)** AC endurance with test -4 V/2 V pulse and 20 ms width was performed to continuously turn on and off the device, **(c)** reliability of the device was examined with weibull's distribution of first 200 cycles showing shape factor of 6 and 4.7 for V_{reset} and V_{set} distribution, and **(d)** a similar reliability study with distribution of I_{set} and I_{reset} at 0.2 V read voltage.

and reliable performance of the system. In Figure 6.4(c), the Weibull's distribution plot against the V_{set} and V_{reset} of the first 200 switching cycles has been demonstrated. The shape factor and voltage spread of 6 and 1.18 V in V_{reset} and 4.7 and 1.28 V in V_{set} indicate the reliable and uniform switching operation. A similar reliability study using Weibull's distribution was performed on the set and reset currents at a read voltage of 0.2 V over 800 cycles where a spread of 0.141 mA in reset current and 0.912 mA in set current can be seen in Figure 6.4(d).

The organic polymer dielectric based memories have always suffered from poor sample yield and various uniformity issues. Sample yield is another prominent yet rarely explored figure of merit, which becomes significant due to stochastic nature of CF formation and rupture process during switching operation. Figure 6.5(a) shows one such variation of V_{set} and V_{reset} of all the fabricated devices on the sample showing 100% sample yield. A marginal variation in switching voltages shown in the curve again verifies a uniform switching performance. The explanation of conduction mechanism of an RRAM device is vital for a proper understanding of its RS behavior, both in set and reset process. The ln *I*-ln *V* plot of the *I*-*V* curve of Figure 6.3(a) with their voltage sweep directions is shown in Figure 6.5(b) and 6.5(c) for positive and negative voltage respectively. SegmentB and SegmentC demonstrate the curve after the set process and follows a linear behavior of current against the voltage, $I \alpha V^1$; m ~ 1 in $I \alpha V^m$, showing a metallic nature of the CF. In SegmentA, the current-voltage relationship is still linear in the lower voltage region

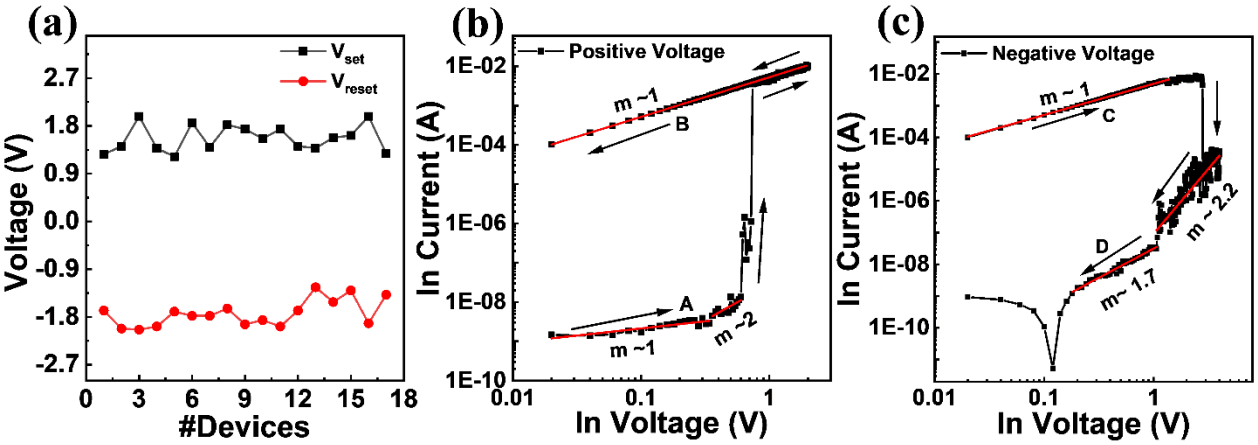

Figure 6.5: (a) V_{reset} and V_{set} data of 17 devices fabricated on Dev.B sample displaying 100% device yield, **(b,c)** log*I*-log*V* curve of switching characteristics to study the conduction mechanism in positive and negative voltages. The slops in regions A, B, C, and D shows ohmic and SCL conduction mechanisms governing during set and reset process.

i.e. m ~ 1 (I α V^1), however; this conduction is attributed to the thermally generated free charge carriers which are dominating the injected charges due to partial filling of trap sites in the bulk. The strong injection at higher voltages results in completely filled-up trap sites and causes the concentration of injected charge carriers to rise higher than thermally generated carriers. This creates a square law dependence of current over the voltage with m ~ 2 (I α V^2, child's law) and creates a space charge. In this region, current is completely controlled by space charge, limiting the further injection of charge carrier into the bulk and the current-voltage relationship can be defined by space charge limited conduction (SCLC) as:

$$J_{sclc} = 9\varepsilon_m \mu \theta V^2 / 8d^3 \qquad (6.1)$$

where ε_m represents the dielectric constant of the material, μ is the mobility of charge carriers, θ is the ratio of free to total carrier density, V the applied bias, and d the separation between two electrodes [Wright, 1961]. After all the trap sites are completely filled, a further increase in voltage will cause a drastic rise in free carriers in bulk and hence increase in current. Similarly, for SegmentD after the reset process, the current-voltage characteristic follows a square-law dependence and indicates the child's law (1<m<2) [B.Schilling, 1970; Saini *et al.*, 2018]. Afterward, the device remains reset and current follows the voltage linearly.

6.3.3 Flexibility Testing of RRAMs

Apart from the electrical performance, another important characteristic of a flexible memory device is its strength to withstand mechanical stress and strain. Initially, the flexibility test on devices was performed by applying the cumulative tensile strain of 0.508%, 0.635%, 0.846%, 1.27%, and 2.54% with bending radii of 12.5 mm, 10 mm, 7.5 mm, 5 mm, and 2.5 mm respectively to the sample for 15 minutes each. Figure 6.6(a) shows the RS characteristics under different bending radii as mentioned above, demonstrating a decent switching performance up to 5 mm radius. The inset shows the sample in bent condition with 2.5 mm radius. Figure 6.6(b) represents the HRS and LRS current variation with different bending radii at 0.2 V read voltage, indicating that the device failed to perform set and reset operation at the 2.5 mm radius. Under the extreme strain conditions, the device performance degraded after 5 mm bending with reset failure at 2.5 mm, demonstrating almost negligible memory window, and an increase in set resistance from 174 Ω in unbent condition to 820 Ω in bent condition. The primary reason behind such failures in flexible RRAMs is the formation of cracks in the active layer, TE, and BE. However, the increased set resistance indicates that the failure is caused by the cracks evolved on the ITO BE (shown in the inset of Figure 6.6(b)) and not on the TE and active layer [Shang *et al.*, 2017]. As displayed in Figure 6.6(c), no significant change in V_{set} and I_{on}/I_{off} is observed, whereas the reset process occurred at wider range of the V_{reset} from -2.66 V to -1.28 V, till the bending radius of 5mm. The device is capable to maintain a memory window of 3×10^3 in 5 mm bending

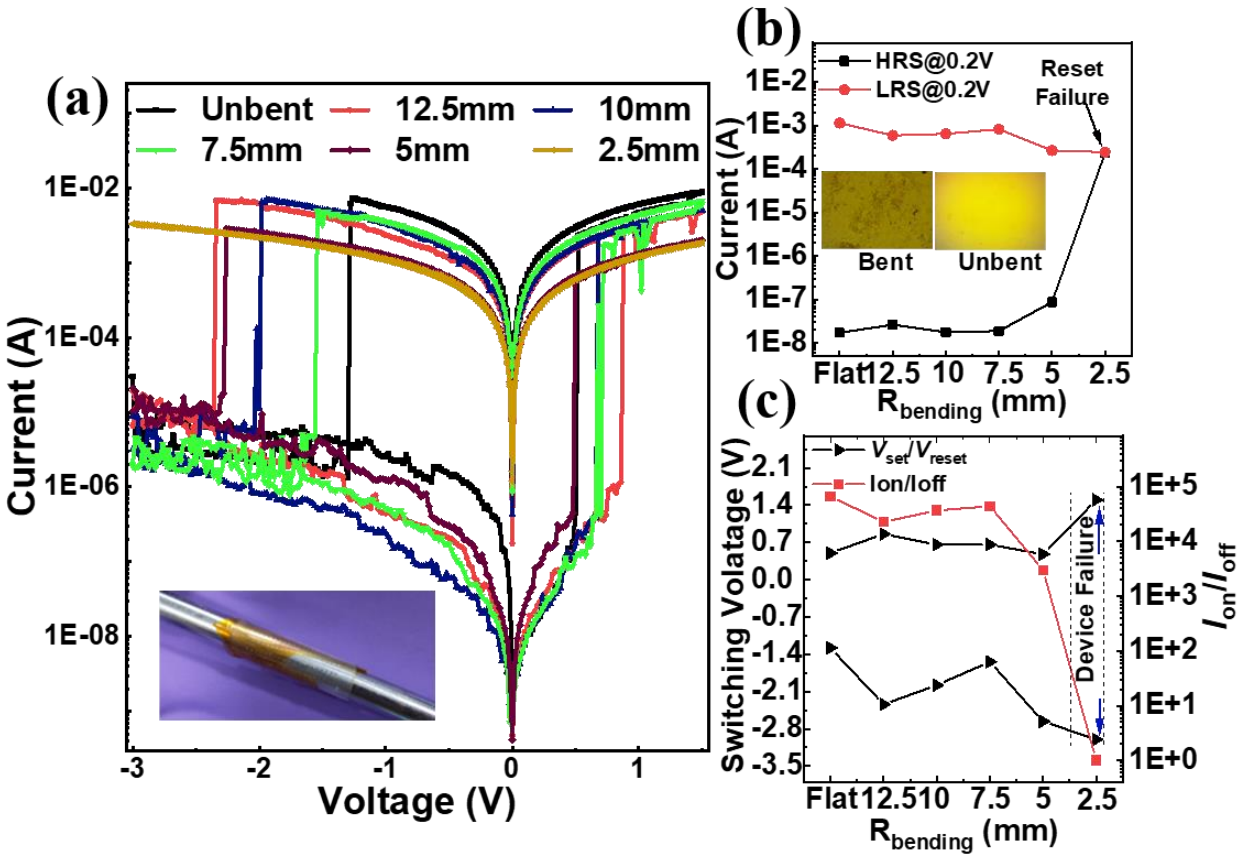

Figure. 6.6(a) Demonstration of switching characteristics after bending the device with bending radius ranging from 12.5 mm to2.5 mm. Inset shows the digital image in bent condition, **(b)** variation of current at 0.2 V read voltage in HRS and LRS at different bending radius with failure at 2.5 mm radius. Inset shows the digital image of cracks evolved at ITO surface after bending and ITO in the unbent condition. **(c)** Variation in V_{set}, V_{reset}, and I_{on}/I_{off} with bending condition varying from unbent to 2.5 mm radius.

condition in comparison to that of 6.7 × 10^4 in the unbent device. After the reset failure in the flexibility test of Dev.B, a similarly fabricated sample was tested for multiple cycles of tensile and compressive strain of ±5 mm radius. The bending scheme of a single cycle is shown in Figure 6.7(a). Figure 6.7(b) displays the *I-V* curve demonstrating the RS characteristics after 10, 20, 50, 100, and 150 cumulative cycles of consecutive tensile and compressive strain by keeping the sample for 5 s in each strained state at 5 mm bending radius. In addition to the excellent switching performance, a similar behavior in switching voltages is observed where the set process occurs at nearly same voltages, whereas a wider range of voltages is observed in the reset. The inset of Figure 6.7(b) indicates the digital image of fabricated sample. Figure 6.7(c) demonstrates the retention time measurements before and after the flexibility test in the HRS and LRS at read voltage of -0.2 V and 0.2 V respectively. With marginal degradation in switching window, yet the two state can be clearly distinguished with I_{on}/I_{off} >10^3, the device successfully demonstrates decent retention time upto 10^4 s. The inset shows variation of HRS and LRS current levels with number of bending cycles at 0.2 V read voltage, again presenting a clear separation between the two states even after the 150 cycles of stress and strain. Figure 6.7(d) shows the variation in various parameters with increasing bending cycles. The device exhibited degradation in memory window from 7.3 × 10^5 in flat condition to 4.2 × 10^3 after initial 20 cycles, however, the same was maintained till the subsequent 150 cycles. Set and reset voltages were also found to be relatively stable after initial variations. These inferences also support earlier observations for flexible devices which reports that major deterioration due to bending in device performance occurs at initial bending application, after which it becomes relatively stabilized [Bharti *et al.*, 2016; Raghuwanshi *et al.*, 2016].

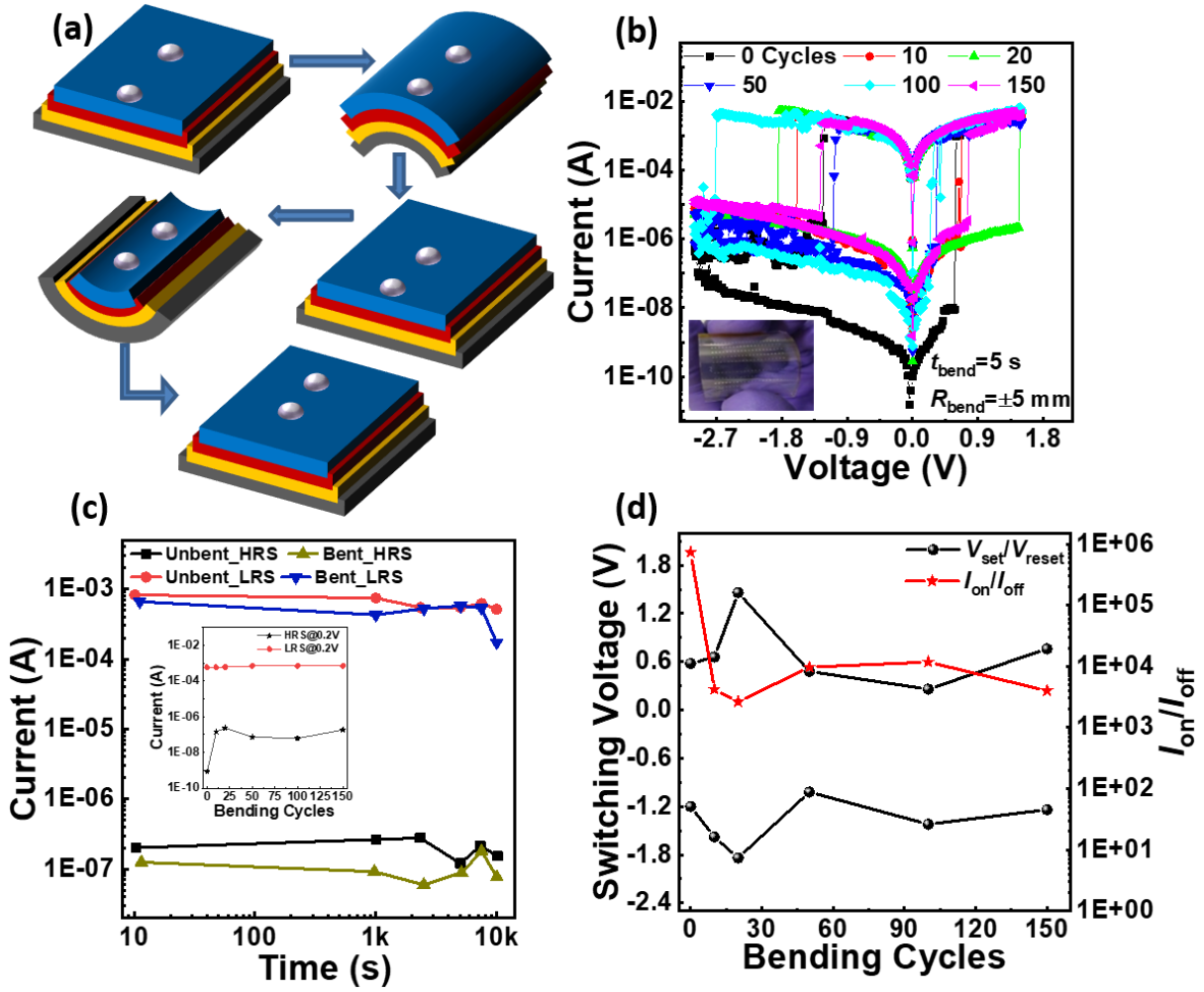

Figure 6.7: (a) The sequence of single tensile stress and strain cycle with bending radius of ±5 mm, **(b)** *I-V* characteristics of device after the test for 150 cycles. Inset shows the digital image of fabricated sample, **(c)** retention characteristics upto 10^4 s at 0.2 V in LRS and -0.2 V in HRS. Inset shows the variation in HRS and LRS current at 0.2 V read voltage with number of bending cycles. **(d)** Variation in V_{set}, V_{reset}, and I_{on}/I_{off} with 150 bending cycles at 5 mm radius.

Table 6.3 enlists some of the recently reported flexible RRAMs with organic, inorganic, and perovskite active layers and associated parameters such as bending radius, number of bending cycles, switching voltages, memory window, and retention time. Most of the flexible RRAMs have been realized on PET or PEN substrates. Most of these RRAMs have shown higher set and reset voltages in comparison to those in the current report, probably due to nonuniformity or higher surface roughness of flexible substrates. In most of these reports, RRAMs have been subjected to mechanical stimulation at large bending radii (lesser strain), which has degraded ON/OFF ratio to less than 10^3. However, RRAMs in the current report have endured a larger mechanical strain (corresponding to smaller bending radius) and despite sustained a larger ON/OFF ratio than those in most of the studies. Retention time of some of the flexible RRAMs (before the flexibility test) is certainly higher, however, that has been obtained at bending radii many folds larger (lesser strain) than that in the current report. Despite the larger strain, RRAMs in the current report have demonstrated a good retention time (after the flexibility test) comparable to that in many reports. All these observations indicate that combined fabrication strategies such as hybrid configuration of organic-inorganic layers and composites of GO and polymers have potential to impart mechanical robustness to the memory devices and can be an excellent choice for producing high performance flexible RRAMs.

Table 6.2 Summary of RRAM devices repsorted with GO or GO based compsosite based active layers.

Dielectric layer	Subs.	Memory Window	V_{set}/ V_{reset} (V)	DC/AC Endurance (cycles)	Retention time (s)	Sample yield (Devices)	Ref.
OCQDs:GO	Rigid	50	~1.5/~-0.9	100	10^4	N/A	[Qi *et al.*, 2018]
PVDF/GO/ PVDF	Rigid	10^3	-2/2.5	N/A	10^4	N/A	[Thakre and Kumar, 2017]
GO:AuNPs	Rigid	10^6	-0.6/0.8	300	10^4	40	[Khurana *et al.*, 2015]
PVA:GO	Rigid	10^4	-0.75/3	1.5×10^4	10^4	N/A	[Sun *et al.*, 2016]
PI/GO:PI/PI	Rigid	10^5	3.5/-3	130	1.4×10^3	N/A	[Wu *et al.*, 2011]
PVA/GO+PVA/ PVA	Rigid	10^4	3.77/-3.17	100	2×10^3	N/A	[Kim *et al.*, 2019b]
PVP/HfO_x	Rigid	80	1.03/-0.68	300/2000	7.2×10^3	75%	[Varun *et al.*, 2018]
PVP:GO/HfO_x	Rigid	3×10^5	0.64/-2.42	800/1400	10^4	17/17	This work

: Composite and / separate layers

Table 6.3 Performance comparison of some recently reported flexible RRAMs

Dielectric layer	Subs.	ON/OFF	V_{set}/ V_{reset} (V)	Bending radius (mm)	Switching/ Bending Cycles @bending redius	Retention time (s)	Ref
GO/TiO_x	PEN	100	-3.2/3.3	6	5000@9 mm	NA	[Nagareddy *et al.*, 2017]
PVOH:$ZnSnO_3$	PET	100	1.5/-1.5	2.5	1500@7.5 mm	10^5	[Siddiqui *et al.*, 2016]
Carboxymethyl cellulose:graphene oxide	PET	$>10^3$	2.22/NA	10	NA	2×10^3	[Liu *et al.*, 2019]
TiO_2/HfO_2	PEN	10	1.6/-1.5	30	100@30 mm	10^4	[Zhang *et al.*, 2019]

Table 6.3 Performance comparison of some recently reported flexible RRAMs

TiO_2	PET	200	1/-0.6	10	500@10	10^5	[Yeom *et al.*, 2017]
PMMA: Graphene:MoS_2	PET	$>10^4$	~-1.5/~1	10	100@10 mm	10 days	[Bhattacharjee *et al.*, 2018]
GO:TiO_2	PET	100	0.52/-0.5	8	10^4@8 mm	NA	[Zhao *et al.*, 2018b]
$CsPbBr_3$/PEDOT:PSS	PET	100	-0.6/1.7	NA	100@18ȏ	NA	[Liu *et al.*, 2017]
PMMA	PEN	10^3	~6/~-7.5	5	400@NA	2500	[Lee *et al.*, 2019c]
Al-In-O/InO	PET	>100	1/-0.5	3.2	500@3.2	10^4	[Duan *et al.*, 2018]
$Cs_3Bi_2I_9$	PET	90	0.5/-0.5	9	100@9 mm	10^4	[Hu *et al.*, 2017]
PVP:GO/HfO_x	PET	4×10^3	0.76/-1.24	5	150@5 mm	10^4	This work

: Composite and / separate layers

6.4 CONCLUSION

In summary, we report on high performance rigid and flexible RRAM devices with PVP:GO and ultra-thin HfO_x hybrid bilayer. Devices fabricated with 1 mg/ml GO concentration demonstrated a uniform and reliable switching performance with excellent repeatability, I_{on}/I_{off} of the order of 10^5, and V_{set} and V_{reset} as low as 0.64 V and -2.42 V respectively on the rigid substrate. The reliability study of the device using Weibull's distribution of set and reset voltages and currents at 0.2 V read voltage indicated a reliable switching operation with marginal variation in these parameters. Finally, flexible PVP:GO/HfO_x devices were examined for their electromechanical strength. With moderate set and reset voltages of 0.5 V and -1.28 V in flat state, these RRAMs maintained a memory window of $>10^3$ even under subjugation of large mechanical strain (corresponding to 5 mm bending radius). After 150 cumulative cycles of consecutive tensile and compressive strain at 5 mm bending radius, flexible RRAMs maintained a clearly distinguishable memory window of 4×10^3 till 10^4 s. These observations indicate that organic-inorganic composite and bilayer based active layers can be an optimum choice for high-performance flexible RRAMs.